Equivalent-circuit model that quantitatively describes domain-wall conductivity in ferroelectric LiNbO₃

Manuel Zahn,[1,2] Elke Beyreuther,[1,*] Iuliia Kiseleva,[1] Ahmed Samir Lotfy,[3]
Conor J. McCluskey,[4] Jesi R. Maguire,[4] Ahmet Suna,[4] Michael Rüsing,[1,5] J. Marty Gregg,[4] and
Lukas M. Eng[1,6]

[1]*Institute of Applied Physics, Technische Universität Dresden, 01062 Dresden, Germany*

[2]*Experimental Physics V, Center for Electronic Correlations and Magnetism, University of Augsburg, 86159 Augsburg, Germany*

[3]*Department of Materials, ETH Zürich, 8093 Zürich, Switzerland*

[4]*Center for Quantum Materials and Technologies, School of Mathematics and Physics, Queen's University Belfast, Northern Ireland*

[5]*Integrated Quantum Optics, Institute for Photonic Quantum Systems (PhoQS), Paderborn University, 33098 Paderborn, Germany*

[6]*ct.qmat: Dresden-Würzburg Cluster of Excellence—EXC 2147, Technische Universität Dresden, 01062 Dresden, Germany*

Ferroelectric domain wall (DW) conductivity (DWC) can be attributed to two separate mechanisms: (a) the injection/ejection of charge carriers across the Schottky barrier formed at the (metal-)electrode-DW junction and (b) the transport of those charge carriers along the DW. Current-voltage (I-U) characteristics, recorded at variable temperatures from LiNbO₃ (LNO) DWs, are clearly able to differentiate between these two contributions. Practically, they allow us to directly quantify the physical parameters relevant to the two mechanisms (a) and (b) mentioned above. These are, for example, the resistance of the DW, the saturation current, the ideality factor, and the Schottky barrier height of the electrode-DW junction. Furthermore, the activation energies needed to initiate the thermally activated electronic transport along the DWs can be extracted. In addition, we show that electronic transport along LNO DWs can be elegantly viewed and interpreted in an adapted semiconductor picture based on a double-diode, double-resistor equivalent-circuit model, the R2D2 model. Finally, our R2D2 model was checked for its universality by successfully fitting the I-U curves of not only z-cut LNO bulk DWs, but equally of z-cut thin-film LNO DWs, and of x-cut thin-film DWs as reported in literature.

DOI: 10.1103/PhysRevApplied.21.024007

I. INTRODUCTION

In the wake of the early prediction of enhanced electrical conductivity along charged ferroelectric domain walls (DWs) in the 1970s [1], the intriguing phenomenon of domain wall conductivity (DWC) has been reported in a number of ferroelectric materials during the last decade, which opens up a unique perspective for designing integrated functional nanoelectronic elements [2,3]. The enormous scientific interest is reflected in several review articles treating fundamental [4–6] and technological [7–9] challenges in understanding and exploiting this type of quasi-two-dimensionally confined electronic transport, which competes with other highly topical low-dimensional electronic systems like graphene, oxide interfaces, or heterointerfaces of classical semiconductors. Notably, DW-based approaches have the ability to write and erase the conducting paths at will within one and the same crystal or thin film.

Among others, conducting DWs in the ferroelectric model system lithium niobate (LiNbO₃, LNO) have attracted concerted interest, since (a) their conductivity can exceed the corresponding bulk values by many orders of magnitude, (b) they are stable across a broad temperature range, and (c) they have already been well described in various previous works [10–14]. Here, fundamental aspects such as the inherent relationship between the DW's geometrical inclination and the resulting electrical conduction, the role of the contact material, the typically nonohmic nature of the respective current-voltage (I-U) characteristics, or signatures for the thermally activated behavior of DW electrical transport have been reported for selected

_____
*elke.beyreuther@tu-dresden.de

samples, albeit for a rather narrow temperature range so far [10,12,15–17]. In parallel, there are a plethora of very recent application-related results already demonstrating single electronic DW-based functionality in either LNO single crystals or thin films, ranging from simple recti-fying junctions [12,18–20] to more complex logic gates [20,21], memristors [22,23], and transistors [21,24,25], to name just a few.

Nevertheless, there are at least two crucial preconditions to meet for proper operation of any reliable LNO-based DW device. First, the related device-specific parameters within an appropriate equivalent circuit have to be quan-tified, including the evaluation of both their general repro-ducibility and their temperature dependence. Second, an in-depth understanding and modeling of the underlying electronic transport mechanism, which has not been com-prehensively addressed so far, has to be achieved. This is precisely the starting point of this work. In order to address the first aspect, we present room-temperature I-U charac-teristics of a set of four virtually identically prepared DWs in single-crystalline 5mol% MgO-doped LiNbO$_3$, postu-late an equivalent-circuit model consisting of a parallel connection of two resistor-diode pairs (the R2D2 model), extract the corresponding resistances, saturation currents, and ideality factors, and discuss their asymmetry relative to the crystal orientation. To deal with the second aspect, we analyze the temperature-dependent current-voltage charac-teristics $I(U, T)$ of two exemplary DWs in detail, which allows us to extract the activation energies for the semi-conductorlike intrinsic DW transport, and the effective Schottky barrier heights of the electrode-DW junction diodes.

Finally, we further test the general applicability of our R2D2 model by analyzing the DWC data not only for z-cut bulk LNO single crystals, but also for DWC observed in z-cut thin-film LNO (TFLN) and literature data on DWC in x-cut LNO.

II. EXPERIMENTAL

A. Preparation of LiNbO$_3$ domain walls with enhanced electrical conductivity

For the present comparative study, four samples were cut from a commercial monodomain, 5mol% MgO-doped, congruent, 200-µm-thick, z-cut LiNbO$_3$ wafer, purchased from Yamaju Ceramics Co., Ltd., polished to optical qual-ity. These crystal pieces measure 5×6 mm^2 along their crystallographic x and y axis, respectively. In what fol-lows, these four samples are labeled DW-01, ..., DW-04. Realizing the protocols described in detail earlier [13,26] and in Sec. A of the Supplemental Material [27], one single hexagonal-shaped reverse-polarized domain was grown by laser-assisted poling within each sample, imaged by polarization-sensitive optical microscopy (see, for example, Fig. S1(b) of the Supplemental Material [27]),

and—after vapor-deposition of macroscopic Cr electrodes onto both crystal surfaces covering the DWs completely [cf. Fig. 2(a)]—electrically tested by acquiring ± 10 V standard I-U characteristics, which revealed a very low, nearly bulklike conductivity with currents in the 0.1 pA range (see Fig. S1(c) of the Supplemental Material [27]).

Subsequently, the DW conductivity was enhanced by ramping up a high voltage (Fig. S1(a) of the Supplemen-tal Material [27]), provided by the voltage source of a Keithley 6517B electrometer, while simultaneously mon-itoring the current flow (Fig. S1(d) of the Supplemental Material [27]) according to Godau *et al.* [13]. As a result, the resistance of the DWs decreased significantly by up to seven orders of magnitude, as exemplified again for sample DW-03 in Fig. 1(a) by the respective I-U characteristics; corresponding data sets for all four samples were recorded as well and will be discussed later in Sec. III A in detail. A stabilization process of the conductivity towards its final magnitude is observed on a time scale of several hours and shown in Fig. 1(b). Thereafter, the conductivity was rechecked and proven to be time-independent for at least 1 month. The exact measurement parameters (voltage sweep velocity, voltage increments, metallic measurement box) were the same as for acquiring the as-grown I-U curves described in Sec. A 2 of the Supplemental Material [27].

Additionally, the three-dimensional internal DW struc-ture of two of the samples (DW-02 and DW-04) were imaged by Cherenkov second-harmonic generation (CSHG) microscopy [28,29], which clearly verified the known relationship between DW inclination and enhanced conduction. For experimental details and images we refer to Sec. B and Fig. S2 in the Supplemental Material [27],
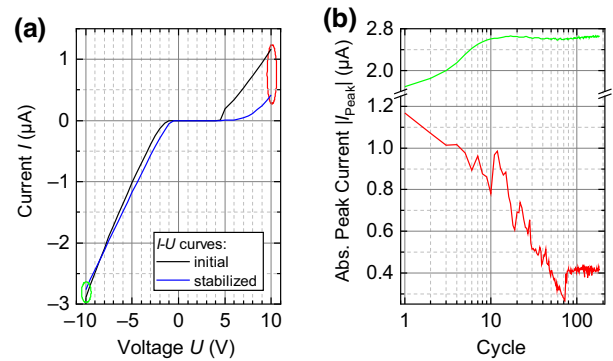

FIG. 1.   Current-voltage (I-U) characteristics and current stabi-lization subsequent of the conductivity enhancement procedure according to Godau *et al.* [13], shown for sample DW-03. (a) First (black) and last (blue) I-U cycle obtained directly after the conductivity enhancement procedure and 9 h later. (b) Evolution of the absolute value of the maximum current at +10 V (red) and −10 V (green) as a function of the number of measurement cycles. The I-U cycles were acquired between −10 V and +10V, setting the measuring voltage in steps of $\Delta U = 0.5$ V with time intervals of 2 s.

the latter showing a decisively altered (i.e., shrunken and inclined) DW shape for the case of DW-02 and a strong structural change for the case of DW-04, which we refer to as "domain explosion", as described and discussed by Kirbus *et al.* [14] earlier.

B. Quantitative analysis of room-temperature current-voltage characteristics: the R2D2 model

Since the typical post-enhancement *I*-*U* characteristics of a LiNbO$_3$ DW with its two Cr electrodes exhibit the shape as shown in Fig. 1(a), including obviously (i) nonohmic, diodelike regions for low voltages, and (ii) linear behavior for higher measurement voltages, with (iii) an additional clear asymmetry with respect to the voltage polarity, we heuristically postulate a parallel connection of two diode-resistor pairs, sketched in Fig. 2(b), as the related equivalent circuit, where one pathway describes the "forward" and one the "backward" behavior along the DW. The four circuit elements are characterized by their resistances R, saturation currents I_s, and ideality factors n, each in forward and backward direction (symbolized by
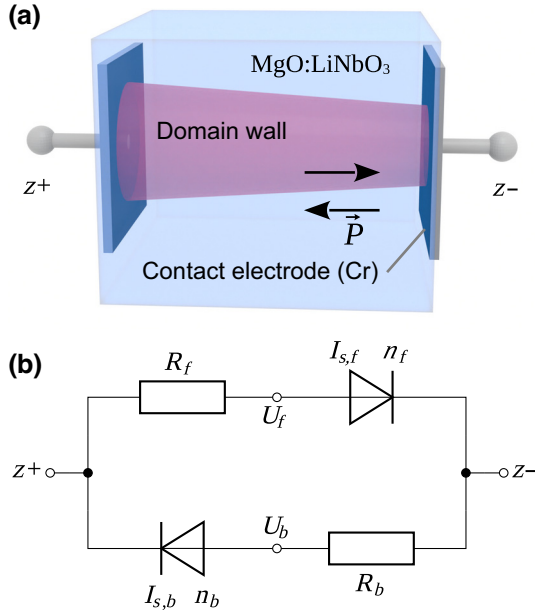

(a)

(b)

FIG. 2. (a) Sketch of the sample configuration: LiNbO$_3$ crystal with an inclined and thus conducting domain wall (DW) structure between two Cr electrodes at the crystal's $z+$ and $z-$ surfaces. (b) Proposed R2D2 equivalent circuit consisting of a parallel connection of two diode-resistor combinations, which describes the *I*-*U* curves of LiNbO$_3$ DWs contacted by Cr electrodes on both ($z+/z-$) crystal sides. The circuit elements can be quantitatively characterized by a nonlinear nodal analysis at the intermediate potential nodes U_f and U_b based on Kirchhoff's law [30] in the way that the resistances R_f and R_b of the resistors as well as saturation currents ($I_{s,f}$, $I_{s,b}$) and ideality factors (n_f, n_b) of the two diodes are extracted from curve-fitting procedures based on Eqs. (1) and (2).

the indices f and b), respectively. To calculate the electric current through the circuit according to Kirchhoff's current law [30], the currents at the nodes with the intermediate potentials U_f and U_b are considered. Due to charge conservation, the currents flowing through the respective resistors and diodes must be equal at these nodes. Formally expressed, there is at least one voltage value $U_f \in [U_{z-}, U_{z+}]$, for which the following relation holds:

$$I_{\text{resistor}} = \frac{U_{z+} - U_f}{R_f} = I_{\text{diode}}(I_{s,f} ; n_f ; U_f - U_{z-}). \quad (1)$$

In the case of a resistor and a diode that both have a monotonic *I*-*U* characteristic, it is exactly one voltage value that exists. Thus, I_{diode} is represented by the well-established Shockley equation [31]:

$$I_{\text{diode}}(I_s; n; U) = I_s \left[\exp\left(\frac{U}{nk_B T} \right) - 1 \right], \quad (2)$$

where k_B is the Boltzmann constant and T is the absolute temperature. This choice of U_f ensures that no charges accumulate at the intermediate node, and that the current flow is time-independent. For U_b and the circuit elements in the backward direction, analogous considerations are taken into account.

Thus the two-resistor, two-diode (R2D2) model exhibits six free parameters (R_f, R_b, $I_{s,f}$, $I_{s,b}$, n_f, n_b), which can be fitted by numerical treatment of Eq. (1). Since the characteristic *I*-*U* curves were defined by more than 40 experimentally obtained measurement points (cf. Sec. II A above and Sec. A 2 of the Supplemental Material [27]), the convergence of the optimization process is achieved. Before applying the fitting routine, parameters were manually adjusted to the right order of magnitude, to ensure convergence. To take account for the possibly broad intervals for the fitting parameters, the logarithm to the base 10 of the parameters' values was optimized instead of the parameters themselves. The optimization was performed using a trust region reflective algorithm [32] with least-squares cost function, as implemented in the Python3 library SCIPY [33].

C. Investigation of the electrical-transport mechanism by temperature-dependent current-voltage curves

In order to (i) figure out the precise electrical transport mechanism through the DW, (ii) to derive the corresponding characteristic parameters such as the activation energy or the barrier height, and (iii) to check for the temperature stability of the circuit parameters in general, temperature-dependent *I*-*U* measurements from 320 K down to around 80 K were performed with two of the four samples, DW-01 and DW-04. A liquid nitrogen bath cryostat (Optistat DN by Oxford Instruments) was used, controlling the temperature by two independent Pt-100 platinum resistance

sensors, one positioned at the heat exchanger and the other directly next to the sample. The operation of the cryostat, comprising gas flow regulation, heating control, and temperature reading at the heat exchanger, was accomplished via an ITC 503 temperature controller by Oxford Instruments, while the Pt-100 sensor near the sample was read out by a Keithley 196 digital multimeter. Full *I-U* characteristics in the ± 10 V range were acquired for 40 different logarithmically distributed temperatures with a Keithley 6517B electrometer in steps of $\Delta U = 0.5$ V with $dU/dt = 0.5$ V/s in two-point geometry with wires shielded up to the probe head. The temperature setpoints were changed stepwise and three *I-U* cycles were recorded, always after reaching thermal equilibrium, that is, after a waiting period of around 30 min when having set a new setpoint temperature. To eliminate transient effects, all subsequent calculations were performed with the third *I-U* cycle only. While changing the temperature, the two electrodes were short-circuited via the electrometer to achieve an equalization of pyroelectrically generated charges. Furthermore, spurious temperature fluctuations during *I-U* measurements were proven to be less than 0.01 K. Thus pyroelectric effects are neglected in all the following evaluations.

In sum, a "three-dimensional" data field $I(U, T)$ with current values I measured at 40×40 voltage-temperature combinations (U, T) was collected (Fig. 3). The *I-U* characteristics at fixed temperature were evaluated analogously to the processing of the room-temperature curves described in Sec. II B. As a result, the temperature dependences of DW resistances $[R_f(T), R_b(T)]$, diode saturation currents $[I_{s,f}(T), I_{s,b}(T)]$, and ideality factors $[n_f(T), n_b(T)]$ could be established. First, the $R(T)$ characteristics were brought to the form of Arrhenius plots $[\ln(R)(1/T)]$, which allowed us to extract the activation energy E_a. In order to decide to which precise $R(T)$ curve form the data should be fitted to extract E_a, a preliminary, tentative evaluation step was carried out. A number of electrical-transport models, such as thermally activated

hopping and different polaron-hopping and variable-range hopping models, were tested for the exemplary case of sample DW-01 with the result that simple thermally activated hopping transport with the following temperature dependence of the conductivity σ (being equivalent to R),

$$\sigma(T) = \tilde{\sigma}_0 \exp\left(-\frac{E_a}{k_B T}\right), \tag{3}$$

where $\tilde{\sigma}_0$ symbolizes a constant prefactor related to the sample geometry, appears to be the most probable process here, which fully agrees with assumptions used by previous authors [12,23]. This allows for a linear fitting of the Arrhenius plots with $-E_a/k_B$ being the slope. The full analysis, including a listing and a short explanation of all models considered, is given in Sec. C of the Supplemental Material [27] (based on the more detailed work of ref. [34], taking into account a number fundamental works on transport phenomena [35–41]).

Second, the curves for the saturation currents $I_s(T)$ were fitted using the theoretical relationship derived from the thermionic emission model, which, in brief, describes the transport across an energy barrier as a combination of thermal activation and tunneling through the latter on the activated energy level (see, for example, Rhoderick and Williams [31]):

$$I_s = A^\star T^2 \exp\left(\frac{-q\Phi_{\text{eff}}}{k_B T}\right), \tag{4}$$

where Φ_{eff} is the effective potential barrier height, and $A^\star$ is a material-specific parameter known as the Richardson constant. Thus, this evaluation supplied us with estimates for the effective Schottky barrier heights of the DW-metal contacts.

III. RESULTS AND DISCUSSION

A. Quantifying resistor and diode parameters from room-temperature current-voltage characteristics

As one key result, Fig. 4 comparatively displays the *I-U* characteristics of the four virtually identically prepared conductive DWs in bulk LNO at room temperature. All curves show clear nonohmic behavior for low measuring voltages and a rather linear progression for higher applied voltages, with a clear asymmetry toward the polarity of the measuring voltage. As indicated in Sec. II B, we fit all four curves according to the R2D2 equivalent-circuit model [Fig. 2(b), Sec. II B] and obtain the numerical values for the six free parameters as summarized in Table I (cf. Table S2 in the Supplemental Material [27] for uncertainties), which we discuss more closely in what follows.

(1) **Resistances.** Typical values between 2.6 and 7.2 MΩ, all within the same order of magnitude, are
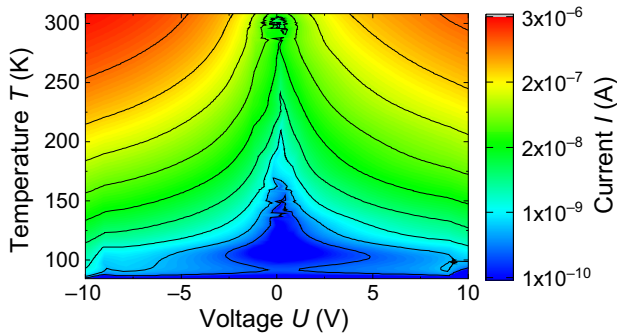

FIG. 3.   Temperature-dependent current-voltage data, depicted as a heat map with 40×40 measured current (absolute) values as a function of both measuring voltage and temperature (data from DW-04).
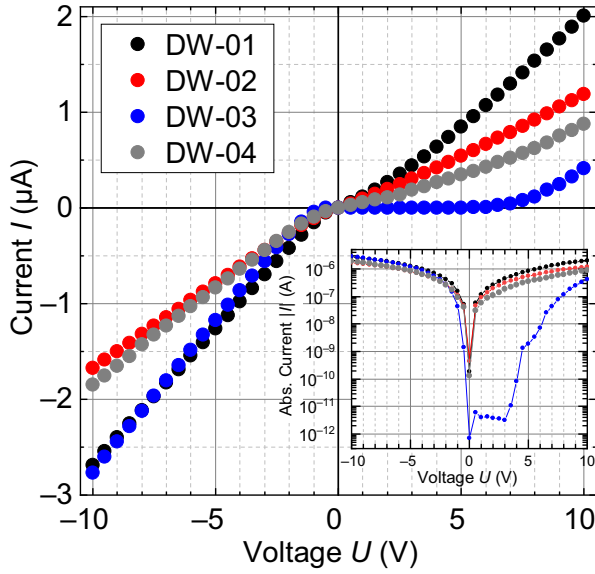
FIG. 4. Room-temperature *I-U* characteristics of a set of four DWs in single-crystal LiNbO₃, contacted macroscopically with vapor-deposited Cr electrodes, all reproducibly revealing a nonohmic and asymmetric DWC. The inset depicts the corresponding semilogarithmic plot (see also Fig. S3 of the Supplemental Material [27] for a closeup view). For both the geometric interpretation and the assigned R2D2 equivalent circuit, which combine ohmic and diodelike character in a single concept, see Fig. 2(b).

observed for R_f and R_b. This also means a conductivity enhancement of seven or eight orders of magnitude as compared to the as-grown DWs before application of the "enhancement" protocol (cf. Fig. S1(c) of the Supplemental Material [27]), which is the expected and desired result due to the enlarged DW inclination with respect to the crystal's z-axis.

(2) **Saturation currents.** Here, a nominally large variation over five orders of magnitude between 10 pA and 1 µA appears at first glance. However, when excluding the $I_{s,f}$ value for DW-03, which is probably caused by a peculiarity in the real structure of the electrode-DW

TABLE I. Equivalent-circuit parameters obtained by modeling the *I-U* characteristics shown in Fig. 4 according to the R2D2 model [Fig. 2(b)] via a least-squares fit based on Kirchhoff's current law. Note that R^2 in the last column denotes the coefficient of determination here. See also Table S2 of the Supplemental Material [27] which additionally tabulates the uncertainties for all fit parameters.

Sample	R_f [MΩ]	$I_{s,f}$ [pA]	n_f	R_b [MΩ]	$I_{s,b}$ [pA]	n_b	R^2
DW-01	3.68	1.23×10^5	35.7	3.44	430	5.33	0.990
DW-02	7.16	9.83×10^4	23.6	5.51	100	5.25	0.980
DW-03	2.84	12.8	33.6	3.07	211	6.41	0.951
DW-04	2.59	3.41×10^5	240	4.48	4913	19.8	0.957

junction as clearly seen from the logarithmic current plot in the inset of Fig. 4 and in Fig. S3 of the Supplemental Material [27], the saturation currents cover only two orders of magnitude.

(3) **Ideality factors.** The values for n_f, n_b are much larger than 2, indicating significant differences between conductance along DWs and conventional semiconductors (with the latter having typical *n* values between 0.5 and 2). However, this phenomenon of anomalously high *n* values also occurs for highly doped semiconductors (for silicon above $N_d \approx 10^{19}$ m⁻³ at 300 K) and is described by the field emission case of the thermionic-emission theory [31]. Transferred to the DW, it indicates a high hopping site density inside the DW that is in agreement with former theoretical calculations on LiNbO₃ [42]. Notably, the ideality factors in the forward direction n_f are much larger than those in the backward direction n_b.

There are natural reasons for the inequality of forward and backward parameters. First, we have the geometrical DW asymmetry between $z+$ and $z-$ sides due to the domain growth process starting from the $z+$ toward the $z-$ side. Second, on an even more fundamental level, the general intrinsic asymmetry of the two different LiNbO₃ surfaces is reflected in their different surface terminations, the different processes of charge compensation, and the subsequent dramatically different ionization energies (6.2 eV versus 4.9 eV) and thus work functions, as shown experimentally by photoelectron spectroscopy in the past [43] and supported by theoretical calculations as well [44–46]. Consequently, it appears logical that these two very different crystal surfaces form clearly distinguishable junctions with the Cr electrodes with side-specific (though not known in detail) electronic-defect state distributions and thus band alignments, which are finally visible as direction-dependent equivalent-circuit parameters.

The rather high coefficient of determination R^2 achieved for all samples indicates that the R2D2 equivalent-circuit model describes the conduction parameters adequately well.

In addition to the two considered current paths, two further channels may contribute to the overall conductance, one having two diodes in opposite directions and one consisting of a single resistor only. While the first path can only weakly conduct due to the reverse-biased diode, the second path would exhibit a purely ohmic *I-U* characteristic, as was observed by Werner *et al.* [12] and Godau *et al.* [13]. Both turned out to be of minor influence in our experiments but cannot be excluded in general.

One may speculate whether there is a fundamental reason why a parallel connection of two current paths appears to be the most suited here. Such reasoning is also motivated by previous results obtained by Godau *et al.* [13] and Wolba *et al.* [47] on the nonuniform local distribution of the conductance. Thus, the current is bound to distinct

channels (preferably along the DW corners) that are separated from each other.

Apart from the above more electrotechnical viewpoint focusing on the circuit-element quantification, we now proceed with the physical interpretation of the suggested circuit elements in the R2D2 model, shown in Fig. 2(b), distributed to the two separate current paths. Heuristically, the diodes represent the Schottky barriers between the metal electrodes and the DW, while the resistors reflect the intrinsic DWC. In the following section, we obtain two more characteristic parameters of the two transport contributions by temperature- dependent *I-U* measurements: (i) the activation energy E_a for the transport along the DW, and (ii) the effective barrier height Φ_{eff} for the metal-DW junction.

B. Analysis of the underlying carrier transport processes through temperature-dependent domain wall current measurements

To achieve an in-depth understanding of both the transport across the Schottky barrier at the two electrode-DW interfaces and along the DW itself, *I-U* characteristics for samples DW-01 and DW-04 at different temperatures between 80 and 320 K were acquired, as exemplified for selected temperatures in Fig. 5(a). Obviously, the current level decreases with decreasing temperature, as is typical for a semiconducting material, while the general shape of the *I-U* characteristics does not significantly change with temperature, showing the same features as discussed in the previous section. Due to the latter fact, we extracted the R, I_s, and n values analogously to the room-temperature parameters, but can now plot them as a function of temperature, as displayed in Figs. 5(b) and 5(c), as well as in Fig. S4 of the Supplemental Material [27], respectively.

First, the resistances R obtained [Fig. 5(b)] follow Arrhenius-like temperature characteristics, as expected. The Arrhenius law is observed across the full temperature range, proving the stability of the intrinsic conduction process, which might be easy to account for in a potential DW nanoelectronic device. The numerically extracted activation energies E_a (shown in Table II) match well between the forward and backward direction for each sample, but differ significantly between samples. Although the exemplary analysis of the $\sigma(T)$ dependence, as discussed in Sec. II C above and Sec. C of the Supplemental Material [27], did not clarify whether we are faced with simple thermal activation, adiabatic or nonadiabatic polaron hopping, there is circumstantial evidence which points toward hopping of small free electron-polarons, as also observed in bulk LNO, being the dominant transport process along the DWs as well. Recent *in situ* strain [48] and Hall-effect [49] experiments on similarly conductivity-"enhanced" DWs showed negative charge carriers to be the majority carriers. Furthermore, the numerical E_a values between 0.101 eV
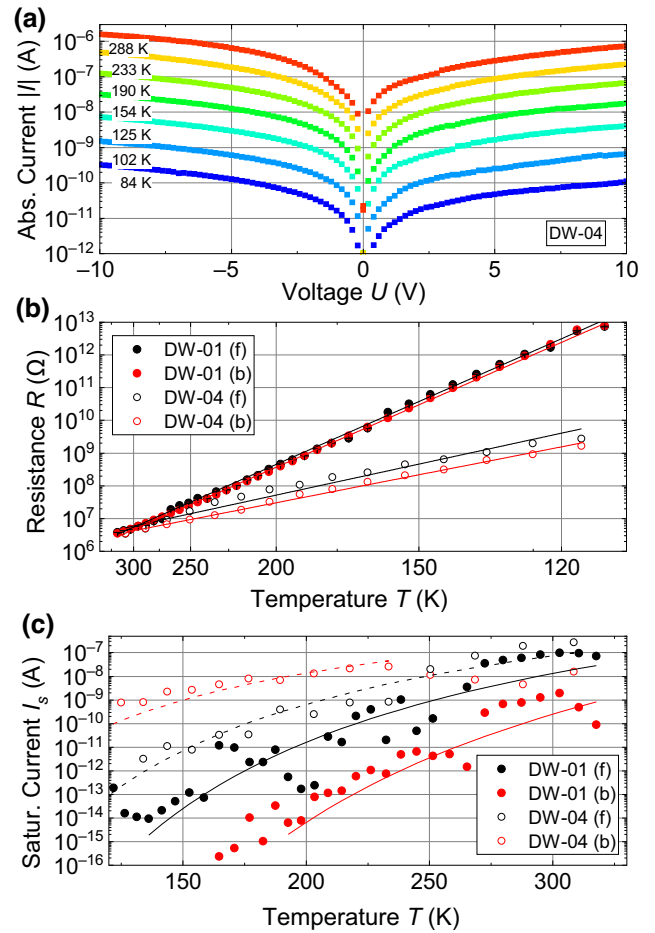
(a)

(b)

(c)

FIG. 5. (a) Temperature-dependent current-voltage curves in logarithmic representation, exemplarily shown for DW-04. Equivalent-circuit parameters (b) R (dots: experimental data, lines: Arrhenius-law fits) and (c) I_s [dots: experimental data, lines: fits according to the thermionic emission model, cf. Eq. (4)] as a function of temperature, which confirm the semiconductorlike intrinsic conductivity in LNO DWs between 110 and 320 K, providing estimates for the activation energies E_a and the effective Schottky barrier heights Φ_{eff} via the respective fit parameters, see Table II. The fits were performed over the respective temperature ranges indicated by the lines only. The fitting ranges had to be limited in this way, since we had to disregard data points of high relative uncertainty. Note the reciprocal scaling of the temperature axis in panel (b).

and 0.229 eV derived here (Table II) are in full accordance with reported activation energies for electron-polaron hopping in bulk LNO, as summarized, for example, in the review article by Reichenbach *et al.* [50], where the (also rather large) interval between 0.1 and 0.24 eV is stated.

Second, the saturation currents I_s of the diode component [Fig. 5(c)] can be satisfactorily fitted by Eq. (4) reflecting the validity of the thermionic emission model for the electrode-DW Schottky contact. The effective Schottky barrier Φ_{eff} is estimated between 0.1 to 0.5 eV (also listed in Table II). A likely source of this rather large range

TABLE II.   Activation energy E_a, Richardson constant $A^\star$, and Schottky barrier height Φ_{eff} tabulated for the two inspected bulk DWs in LNO, as derived from the curve fits of $R_{f,b}(T)$ and $I_{s;f,b}(T)$ in Figs. 5(b) and 5(c).

Sample	E_a [eV]	$A^\star$ [nA K^{-2}]	Φ_{eff} [eV]
DW-01 (f)	0.2291 ± 0.0010	775 ± 1954	0.50 ± 0.05
DW-01 (b)	0.2290 ± 0.0016	19 ± 32	0.305 ± 0.029
DW-04 (f)	0.1008 ± 0.0019	0.16 ± 0.28	0.106 ± 0.020
DW-04 (b)	0.107 ± 0.005	2.1 ± 2.89	0.203 ± 0.022

are variations of the individual electronic-defect state distribution at the metal-DW interface introduced during the metal-electrode deposition and conductivity enhancement procedure, whereas the latter has the decisively larger impact [51]. An interpretation of the extract Richardson constants $A^\star$, which vary over three orders of magnitude, is not easy, since they depend on several barely known quantities such as the relative electron mass $m^\star$ and the barrier cross-section width. In all four cases examined, the uncertainty of $A^\star$ seems to be heavily overestimated due to the exponential transformation, while $\log_{10}(A^\star)$ is still a well-defined quantity with a relative uncertainty of less than 10%.

Third, the evaluation of the ideality factors n presents a more ambiguous picture (see Fig. S4 of the Supplemental Material [27]). Based on the thermionic-emission theory, only a very weak temperature dependence is expected for the ideality factors due to changes of the effective electron mass [31,52]. Furthermore, the ideality factor strongly depends on the effective hopping site density, which is independent of temperature. However, apart from the case of sample DW-01 in the backward direction, which indeed shows a rather constant value over the covered temperature range, the results for the remaining cases exhibit rather strong fluctuations between 15 and above 80, caused by the fragile position of n within the argument of the exponential function. On the other hand, even the quite scattered data support the trend toward n values being considerably larger than for standard semiconductor diodes.

As an interesting and illustrative side note, the acquired three-dimensional data set $I(U, T)$, plotted as a heat map in Fig. 3, allows the activation energy E_a to be extracted directly as the slope from the $\ln(I)(1/T)$ current-versus-temperature curves. These values are shown in Fig. 6, plotted as a function of measuring voltage U, together with the partial fits to the theoretical $E_a(U)$ dependence. Based on Eq. (3), the latter is obtained by calculating the partial derivative of $\ln I$ with respect to $1/T$, as worked out in detail in Sec. G of the Supplemental Material [27], using Eqs. (2) and (4), finally resulting in

$$E_a := -k_B \frac{\partial \ln I}{\partial 1/T} = E_0 - A \cdot \frac{U/U_c}{1 - \exp(-U/U_c)}, \quad (5)$$
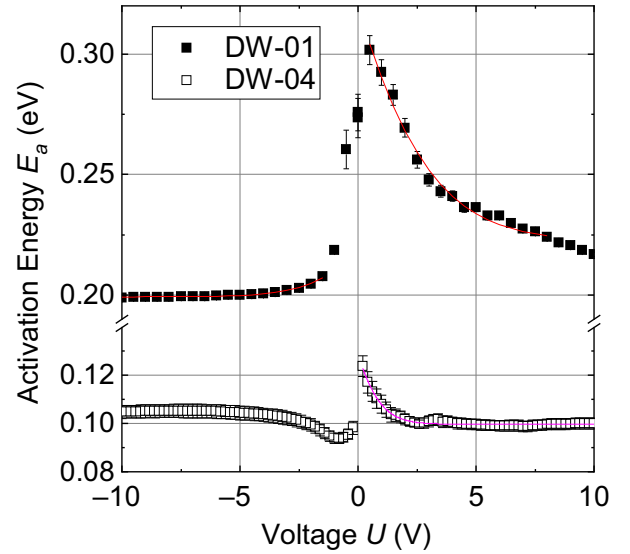

FIG. 6.   Activation energies, as derived from the currents' Arrhenius plots, as a function of the measuring voltage: dots reflect the experimental data, solid lines the fit curves according to Eq. (5).

with the fit parameters E_0, A, and U_c. However, the qualitative agreement of the experimental $E_a(U)$ curve with the (partial) fits according to Eq. (5) is convincing for both samples. The curves show a characteristic strong increase of E_a at low voltages, which clearly supports our central assumption that at low fields the barrier at the electrode-DW junction dominates the transport behavior of the electrode-DW system. The significant difference of the constant activation energy at large electric fields between 0.10 and 0.22 eV for the two tested DWs is astonishing at first glance, but is in full agreement with the activation energies derived from the Arrhenius plots of the resistances before, which show nearly the same rather different values for the two inspected samples. We refrain from discussing the fit parameters E_0, A, and U_c in detail, since they refer to a kind of effective temperature and thus their strict physical meaning is not straightforward to determine.

C. Applying the R2D2 model to domain wall conductance in thin-film LiNbO₃

To test whether or not our R2D2 model is of general use for interpreting DWC, here we analyze the DWC from two distinctly different samples:

(1) DW arrays that have been written into a z-cut, 500-nm-thin TFLN sample using a larger bias voltage applied to the tip of a scanning force microscope (for details see Sec. H of the Supplemental Material [27] and ref. [53]). We processed these I-U characteristics of the DW array shown in Fig. 7 in the same way as accomplished for the I-U curves in Fig. 4. The curve fitting (for a summary of
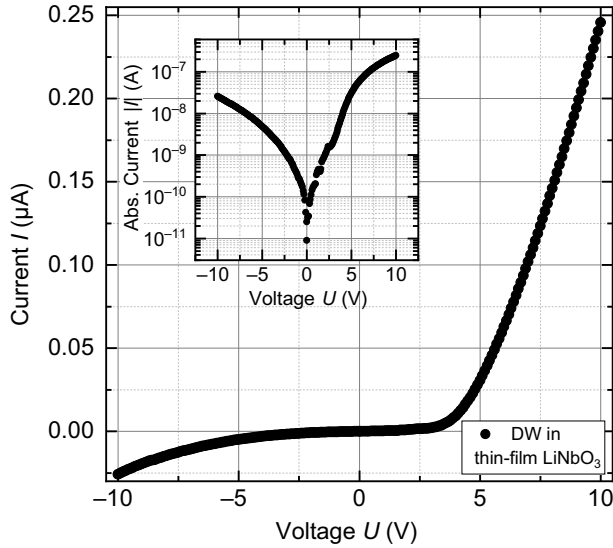
FIG. 7.   Current-voltage characteristics of a thin-film LiNbO$_3$ DW induced by an atomic force microscopy tip, contacted with Ag electrodes, revealing a nonohmic and asymmetric current, depicted as linear and semilogarithmic (inset) plot.

all results refer to Table S3 of the Supplemental Material [27]) succeeded with an excellent R^2 value of 0.999 95, resulting in resistances being a factor of 10 larger than observed for the single-crystal DWCs (i.e., $R_f = 18$ MΩ and $R_b = 94$ MΩ), and diode saturation currents being smaller on trend (i.e., $I_{s,f} = 16$ pA and $I_{s,b} = 507$ pA). The extracted values of the forward and backward diode ideality factors, which are $n_f = 23$ and $n_b = 76$, were a surprise in comparison to the single-crystal results, where n_f appears to be systematically larger than n_b. Thus, the data might indicate a different mechanism responsible for the directional asymmetry in the thin-film sample, which is supported by the findings by Suna *et al.* [20] showing that near-surface DW bending results in a significant contribution to the diode like response. Nevertheless, an in-depth clarification needs a more systematic approach, which is outside the scope of the present study.

(2) We applied the R2D2 model to literature DWC data that were recorded at DWs in an *x*-cut TFLN sample by Qian *et al.* [19]. The analysis of these data results in resistances in the gigaohm range, I_s values in the picoampere range, and similarly high ideality factors as above, all of them with satisfying R^2 values as well (see Table S4 of the Supplemental Material [27] for the numerical values).

IV. SUMMARY AND OUTLOOK

In this study, ferroelectric conductive domain walls (CDWs) were engineered into 200-μm-thick 5mol% MgO-doped LiNbO$_3$ single crystals and contacted by macroscopic vapor-deposited chromium electrodes at both

crystal sides. Current-voltage (*I-U*) characteristics in the ± 10 V range were recorded comparatively at a set of four such CDWs, which exhibited reproducibly asymmetric nonohmic characteristics. Thus, an equivalent-circuit model, the R2D2 model consisting of a parallel connection of two resistor-diode pairs, was postulated empirically, which allowed us to fit the *I-U* curves using Kirchhoff's current law together with Shockley's diode equation, ending up in a systematic quantification of typical resistance ranges and diode parameters (saturation current, ideality factor) for this specific DW-electrode configuration in the forward and backward direction, which indeed showed systematically different values due to the intrinsically unequal crystallographic and electrochemical behavior of the $z+$ and $z-$ LiNbO$_3$ surfaces. The model was also successfully applied to exemplary *I-U* characteristics of differently created DWs in TFLN and might be generally usable within a standardized analysis routine of DW-related *I-U* characteristics in the future.

From additional temperature-dependent *I-U* recordings at two selected CDWs, we empirically assigned (i) the diodic (nonlinear) part around zero measuring voltage to the influence of the CDW-electrode junction showing thermionic emission in the vicinity of a Schottky barrier, and (ii) the ohmic (linear) part at higher bias voltages to the intrinsic conduction within the DW. The latter was further identified to behave like a thermally activated semiconductor, with activation energies between 100 and 230 meV, which quantitatively match free electron-polaron hopping, as derived from the slope of the linear Arrhenius plots of resistances. Finally the effective Schottky barrier heights of the DW-electrode junctions were derived from the temperature dependence of the diode saturation currents.

Our results raise a number of questions to be addressed in the future. First, the microscopic nature of the electric-current paths along the CDWs was not completely clarified due to the utilization of macroscopic electrodes. Here, a complementary investigation based on scanning probe microscopy, especially employing conductive atomic force microscopy to directly contact different regions of the DW by the tip and capture local *I-U* characteristics, is needed, which could potentially lead to a more generalized equivalent-circuit model. Second, from a statistical point of view, an investigation of a decisively broader set of CDWs including *I-U* and CSHG microscopy data of all specimens would allow us to correlate all relevant DW fabrication parameters to the final electrical performance in terms of the equivalent-circuit parameters and to substantiate functional structure-property relationships. Having disentangled two different conduction contributions, a third future challenge is the control and optimization of the electrode-DW junction by varying the contact metal on the one hand and by a higher degree of automatization during the preparation process on the other hand.

ACKNOWLEDGMENTS

---

[1] B. M. Vul, G. M. Guro, and I. I. Ivanchik, Encountering domains in ferroelectrics, Ferroelectrics **6**, 29 (1973).

[2] G. Catalan, J. Seidel, R. Ramesh, and J. F. Scott, Domain wall nanoelectronics, Rev. Mod. Phys. **84**, 119 (2012).

[3] D. Meier, Functional domain walls in multiferroics, J. Phys.: Condens. Matter **27**, 463003 (2015).

[4] T. Sluka, P. Bednyakov, P. Yudin, A. Crassous, and A. Tagantsev, in *Topological Structures in Ferroic Materials: Domain Walls, Vortices and Skyrmions*, edited by J. Seidel (Springer International Publishing, Cham, 2016), p. 103.

[5] P. S. Bednyakov, B. I. Sturman, T. Sluka, A. K. Tagantsev, and P. V. Yudin, Physics and applications of charged domain walls, npj Comput. Mater. **4**, 65 (2018).

[6] G. Nataf, M. Guennou, J. Gregg, D. Meier, J. Hlinka, E. K. H. Salje, and J. Kreisel, Domain-wall engineering and topological defects in ferroelectric and ferroelastic materials, Nat. Rev. Phys. **2**, 634 (2020).

[7] P. Sharma, P. Schoenherr, and J. Seidel, Functional ferroic domain walls for nanoelectronics, Materials **12**, 2927 (2019).

[8] D. Meier and S. Selbach, Ferroelectric domain walls for nanotechnology, Nat. Rev. Mater. **7**, 157 (2021).

[9] P. Sharma, T. S. Moise, L. Colombo, and J. Seidel, Roadmap for ferroelectric domain wall nanoelectronics, Adv. Funct. Mater. **32**, 2110263 (2022).

[10] M. Schröder, A. Haußmann, A. Thiessen, E. Soergel, T. Woike, and L. M. Eng, Conducting domain walls in lithium niobate single crystals, Adv. Funct. Mater. **22**, 3936 (2012).

[11] M. Schröder, X. Chen, A. Haußmann, A. Thiessen, J. Poppe, D. A. Bonnell, and L. M. Eng, Nanoscale and macroscopic electrical ac transport along conductive domain walls in lithium niobate single crystals, Mater. Res. Express **1**, 035012 (2014).

[12] C. S. Werner, S. J. Herr, K. Buse, B. Sturman, E. Soergel, C. Razzaghi, and I. Breunig, Large and accessible conductivity of charged domain walls in lithium niobate, Sci. Rep. **7**, 9862 (2017).

[13] C. Godau, T. Kämpfe, A. Thiessen, L. M. Eng, and A. Haußmann, Enhancing the domain wall conductivity in lithium niobate single crystals, ACS Nano **11**, 4816 (2017).

[14] B. Kirbus, C. Godau, L. Wehmeier, H. Beccard, E. Beyreuther, A. Haußmann, and L. M. Eng, Real-time 3D imaging of nanoscale ferroelectric domain wall dynamics in lithium niobate single crystals under electric stimuli: Implications for domain-wall-based nanoelectronic devices, ACS Appl. Nano Mater. **2**, 5787 (2019).

[15] V. Y. Shur, I. S. Baturin, A. R. Akhmatkhanov, D. S. Chezganov, and A. A. Esin, Time-dependent conduction current in lithium niobate crystals with charged domain walls, Appl. Phys. Lett. **103**, 102905 (2013).

[16] X. Chai, J. Lian, C. Wang, X. Hu, J. Sun, J. Jiang, and A. Jiang, Conductions through head-to-head and tail-to-tail domain walls in LiNbO$_3$ nanodevices, J. Alloys Compd. **873**, 159837 (2021).

[17] W. Geng, J. He, X. Qiao, L. Niu, C. Zhao, G. Xue, K. Bi, L. Mei, X. Wang, and X. Chou, Conductive domain-wall temperature sensors of LiNbO$_3$ ferroelectric single-crystal thin films, IEEE Electron Device Lett. **42**, 1841 (2021).

[18] W. Zhang, C. Wang, J.-W. Lian, J. Jiang, and A.-Q. Jiang, Erasable ferroelectric domain wall diodes, Chin. Phys. Lett. **38**, 017701 (2021).

[19] Y. Qian, Y. Zhang, J. Xu, and G. Zhang, Domain-wall p-n junction in lithium niobate thin film on an insulator, Phys. Rev. Appl. **17**, 044011 (2022).

[20] A. Suna, C. J. McCluskey, J. R. Maguire, K. M. Holsgrove, A. Kumar, R. G. P. McQuaid, and J. M. Gregg, Tuning local conductance to enable demonstrator ferroelectric domain wall diodes and logic gates, Adv. Phys. Res. **2**, 2200095 (2023).

[21] J. Sun, Y. Li, Y. Ou, Q. Huang, X. Liao, Z. Chen, X. Chai, X. Zhuang, W. Zhang, C. Wang, J. Jiang, and A. Jiang, In-memory computing of multilevel ferroelectric domain wall diodes at LiNbO$_3$ interfaces, Adv. Funct. Mater. **32**, 2207418 (2022).

[22] P. Chaudhary, H. Lu, A. Lipatov, Z. Ahmadi, V. McConville, A. Sokolov, J. Shield, A. Sinitskii, J. Gregg, and A. Gruverman, Low-voltage domain-wall LiNbO$_3$ memristors, Nano Lett. **20**, 5873 (2020).

[23] T. Kämpfe, B. Wang, A. Haussmann, L.-Q. Chen, and L. M. Eng, Tunable non-volatile memory by conductive ferroelectric domain walls in lithium niobate thin films, Crystals **10**, 804 (2020).

[24] J. P. V. McConville, H. Lu, B. Wang, Y. Tan, C. Cochard, M. Conroy, K. Moore, A. Harvey, U. Bangert, L.-Q. Chen, A. Gruverman, and J. M. Gregg, Ferroelectric domain wall memristor, Adv. Funct. Mater. **30**, 2000109 (2020).

[25] X. Chai, J. Jiang, Q. Zhang, X. Hou, F. Meng, J. Wang, L. Gu, D. W. Zhang, and A. Q. Jiang, Nonvolatile ferroelectric field-effect transistors, Nat. Commun. **11**, 2811 (2020).

[26] C. Godau, Ph.D. thesis, Technische Universität Dresden, Dresden, 2018. https://nbn-resolving.org/urn:nbn:de:bsz:14-qucosa2-709911.

[27] See Supplemental Material at http://link.aps.org/supplemental/10.1103/PhysRevApplied.21.024007 for further details on sample preparation and imaging, additional current-voltage data, as well as extensive curve fit data.

[28] T. Kämpfe, P. Reichenbach, M. Schröder, A. Haussmann, L. M. Eng, T. Woike, and E. Soergel, Optical

three-dimensional profiling of charged domain walls in ferroelectrics by cherenkov second-harmonic generation, Phys. Rev. B **89,** 035314 (2014).

[29] T. Kämpfe, P. Reichenbach, A. Haussmann, T. Woike, E. Soergel, and L. M. Eng, Real-time three-dimensional profiling of ferroelectric domain walls, Appl. Phys. Lett. **107,** 152905 (2015).

[30] E. Lipiansky, *Electrical, Electronics, and Digital Hardware Essentials for Scientists and Engineers* (Wiley, Hoboken, NJ, 2013).

[31] E. H. Rhoderick and R. H. Williams, *Metal-Semiconductor Contacts*, Monographs in Electrical and Electronic Engineering No. 19 (Clarendon Press, Oxford, 1988), 2nd ed.

[32] M. A. Branch, T. F. Coleman, and Y. Li, A subspace, interior, and conjugate gradient method for large-scale bound-constrained minimization problems, SIAM J. Sci. Comput. **21,** 1 (1999).

[33] R. Johansson, *Numerical Python, Scientific Computing and Data Science Applications with Numpy, SciPy and Matplotlib* (Apress, New York, 2019), 2nd ed.

[34] M. Zahn, Master's thesis, Technische Universität Dresden, 2022. https://nbn-resolving.org/urn:nbn:de:bsz:14-qucosa2-776392.

[35] R. Hoffmann, How chemistry and physics meet in the solid state, Angewan. Chem., Int. Ed. **26,** 846 (1987).

[36] S. Baranovski, *Charge Transport in Disordered Solids with Applications in Electronics* (Wiley, Chichester, England, 2006).

[37] A. Miller and E. Abrahams, Impurity conduction at low concentrations, Phys. Rev. **120,** 745 (1960).

[38] N. F. Mott, Conduction in non-crystalline materials, Philos. Mag. **19,** 835 (1968).

[39] A. L. Efros and B. I. Shklovskii, Coulomb gap and low temperature conductivity of disordered systems, J. Phys. C: Solid State Phys. **8,** L49 (1975).

[40] N. F. Mott and E. A. Davis, *Electronic Processes in Non-Crystalline Materials*, International Series of Monographs on Physics (Oxford University Press, Oxford, 2012).

[41] R. Laiho, K. G. Lisunov, E. Lähderanta, M. A. Shakhov, V. N. Stamov, V. S. Zakhvalinskii, V. L. Kozhevnikov, I. A. Leonidov, E. B. Mitberg, and M. V. Patrakeev, Mechanisms of hopping conductivity in weakly doped $La_{1-x}Ba_xMnO3$, J. Phys.: Condens. Matter **17,** 3429 (2005).

[42] E. A. Eliseev, A. N. Morozovska, G. S. Svechnikov, V. Gopalan, and V. Y. Shur, Static conductivity of charged domain walls in uniaxial ferroelectric semiconductors, Phys. Rev. B **83,** 235313 (2011).

[43] W.-C. Yang, B. J. Rodriguez, A. Gruverman, and R. J. Nemanich, Polarization-dependent electron affinity of $LiNbO_3$ surfaces, Appl. Phys. Lett. **85,** 2316 (2004).

[44] R. Hölscher, S. Sanna, and W. G. Schmidt, Adsorption of OH and H at the $LiNbO_3(0001)$ surface, Phys. Status Solidi C **9,** 1361 (2012).

[45] R. Hölscher, W. G. Schmidt, and S. Sanna, Modeling $LiNbO_3$ surfaces at ambient conditions, J. Phys. Chem. C **118,** 10213 (2014).

[46] S. Sanna, R. Hölscher, and W. Schmidt, Temperature dependent $LiNbO_3(0001)$: Surface reconstruction and surface charge, Appl. Surf. Sci. **301,** 70 (2014).

[47] B. Wolba, J. Seidel, C. Cazorla, C. Godau, A. Haussmann, and L. M. Eng, Resistor network modeling of conductive domain walls in lithium niobate, Adv. Electron. Mater. **4,** 1700242 (2018).

[48] E. Singh, H. Beccard, Z. H. Amber, J. Ratzenberger, C. W. Hicks, M. Rüsing, and L. M. Eng, Tuning domain wall conductivity in bulk lithium niobate by uniaxial stress, Phys. Rev. B **106,** 144103 (2022).

[49] H. Beccard, E. Beyreuther, B. Kirbus, S. D. Seddon, M. Rüsing, and L. M. Eng, Hall mobilities and sheet carrier densities in a single $LiNbO_3$ conductive ferroelectric domain wall, Phys. Rev. Appl. **20,** 064043 (2023).

[50] P. Reichenbach, T. Kämpfe, A. Haußmann, A. Thiessen, T. Woike, R. Steudtner, L. Kocsor, Z. Szaller, L. Kovács, and L. M. Eng, Polaron-mediated luminescence in lithium niobate and lithium tantalate and its domain contrast, Crystals **8,** 214 (2018).

[51] I. Kiseleva, Master's thesis, Technische Universität Dresden, 2023. https://nbn-resolving.org/urn:nbn:de:bsz:14-qucosa2-876252.

[52] M. Rudan, *Physics of Semiconductor Devices*, Springer eBook Collection (Springer, Cham, 2018), 2nd ed.

[53] C. J. McCluskey, M. G. Colbear, J. P. V. McConville, S. J. McCartan, J. R. Maguire, M. Conroy, K. Moore, A. Harvey, F. Trier, U. Bangert, A. Gruverman, M. Bibes, A. Kumar, R. G. P. McQuaid, and J. M. Gregg, Ultrahigh carrier mobilities in ferroelectric domain wall corbino cones at room temperature, Adv. Mater. **34,** 2204298 (2022).